Absolute high-resolution Se^{+} photoionization cross-section measurements with Rydberg-series analysis

D. A. Esteves, R. C. Bilodeau, N. C. Sterling, R. A. Phaneuf, A. L. D. Kilcoyne, E. C. Red,
and A. Aguilar

Absolute High-Resolution Se$^+$ Photoionization Cross-Section Measurements with Rydberg Series Analysis

D.A. Esteves,[1,3,†] R.C. Bilodeau,[2,3] N.C. Sterling,[4,‡] R.A. Phaneuf,[1] A.L.D. Kilcoyne,[3] E.C. Red,[3,§] and A. Aguilar[3,*]

[1]*University of Nevada, Reno, Department of Physics, MS 0220, Reno, NV, 89557, USA*
[2]*Western Michigan University, MS 5252, 1903 W. Michigan Ave, Kalamazoo, MI 49008*
[3]*The Advanced Light Source, Lawrence Berkeley National Laboratory, Berkeley, CA, 94720, USA*
[4]*Department of Physics and Astronomy, Michigan State University, 3248, Biomedical Physical Sciences, East Lansing, MI 48824-2320, USA*

Absolute single photoionization cross-section measurements for Se$^+$ ions were performed at the Advanced Light Source (ALS) at Lawrence Berkeley National Laboratory using the photo-ion merged beams technique. Measurements were made at a photon energy resolution of 5.5 meV from 17.75 eV to 21.85 eV spanning the $4s^2 4p^3$ $^4S^o_{3/2}$ ground state ionization threshold and the $^2P^o_{3/2}$, $^2P^o_{1/2}$, $^2D^o_{5/2}$, and $^2D^o_{3/2}$ metastable state thresholds. Extensive analysis of the complex resonant structure in this region identified numerous Rydberg series of resonances and obtained the Se^{2+} $4s^2 4p^2$ $^3P_2$ and $4s^2 4p^2$ $^1S_0$ state energies. In addition, particular attention was given to removing significant effects in the measurements due to a small percentage of higher-order undulator radiation.

PACS number(s): 32.80.Fb, 32.80.Aa, 32.70.Cs, 95.30.Dr, 95.30.Ky

[†] Present Address: JILA, University of Colorado, Boulder, CO, 80304, USA

[‡] NSF Astronomy and Astrophysics Postdoctoral Fellow

[§] Present Address: Department of Physics, Morehouse College, Atlanta, GA, 30314, USA

[*] Electronic address: AAguilar@lbl.gov

I. INTRODUCTION

The interaction of photons with atomic and molecular ions is a fundamental physical process in many important plasma environments such as stars, nebulae and thermonuclear fusion reactions. A powerful tool for exploring these interactions is photo-ion spectroscopy, where a beam of ions interacts with an intense beam of synchrotron radiation.

In the present analysis, absolute single photoionization cross-section measurements of Se^+ are presented at 5.5 meV photon energy resolution in the energy region of the ground state configuration threshold. This work is part of a broader investigation of absolute photoionization cross-section measurements of Se^+ through Se^{5+} and supplements previous lower energy resolution measurements on the same system by Sterling *et al*. [1] (hereafter Paper I). In Paper I, some resonance structures were clearly unresolved, precluding precise assignments for those features. In addition, after the publication of Paper I the possibility of errors in absolute measurements due to higher-order radiation in the photon beam at these very low beamline energies became a concern. The principal motivation of the present work is to augment the resonance analysis of Paper I with high photon energy resolution measurements, and to quantify and address complications that arise from higher-order radiation. With these new measurements we have successfully analyzed the rich and complex resonance structure of Se^+ in the ground state configuration threshold region, have unambiguously identified structures produced by higher-order photons and have corrected the absolute photoionization spectrum for their effects.

The measurements of Paper I were motivated by the detection of Se emission lines in a large number of ionized astrophysical nebulae [e.g., 2,3,4]. The determination of elemental abundances from such observations requires corrections for ionization processes involving unobserved charged states, and hence knowledge of the ionization balance. Photoionization cross sections are a critical piece of atomic data needed to solve for the ionization equilibrium in photoionized nebulae [5]. For a more detailed discussion of the astrophysical background that motivated these measurements, we refer the reader to Sterling *et al*. [6] and Paper I.

II. EXPERIMENT

Measurements were conducted at the Advanced Light Source (ALS) of Lawrence Berkeley National Laboratory using the Ion Photon Beam (IPB) end station permanently installed at undulator Beamline 10.0.1, which utilizes the merged beams photo-ion technique [7]. A detailed description of the IPB apparatus was given by Covington *et al*. [8], with recent modifications described by Alna'Washi *et al.* [9].

Se ions were produced by placing pellets of solid Se within an all-permanent-magnet Electron Cyclotron Resonance (ECR) ion source similar to that reported by Broetz *et al*. [10] and Trassl *et al*. [11]. The amplified 10 GHz input power to the ECR ion source was sufficient to both vaporize and ionize the solid Se, producing a heterogeneous plasma of positive Se ions. These ions were accelerated out of the source and formed into a beam via a 4 kV potential difference. The beam was focused and collimated using an electrostatic einzel lens, two-dimensional steering plates and adjustable horizontal and vertical slits and subsequently mass-to-charge analyzed by a 60º dipole magnet. The ion

source RF amplifier power was approximately 1 Watt which produced a Se^+ primary ion beam with a current between 12 and 16 nA. The resulting 4 keV Se^+ primary ion beam was directed onto the axis of the counter-propagating photon beam using spherical-section electrostatic 90° deflectors. The ion and photon beams were then spatially merged within a well-characterized interaction region as detailed below. A 45° dipole magnet downstream of the interaction region was used to demerge the ions from the photon beam and separate the Se^{2+} photo-ion product beam from the Se^+ primary ion beam. The primary beam current was monitored on a Faraday cup housed within the demerger magnet while the product beam was passed to a set of 90° spherical-section electrostatic deflectors, which directed the product ions onto a stainless steel plate. Secondary electrons produced when the product ions impacted the plate surface were then accelerated into a single-particle channeltron detector and counted. A small background of Se^{2+} ions produced by collision with residual gas in the interaction region at a typical pressure of 5×10^{-10} torr were accounted for by mechanically chopping the photon beam during the measurements.

The present photoionization measurements were made using the IPB end station in *absolute mode*. The typical procedure for absolute mode is to tune the ion and photon beams for spatial overlap within a 29.4 cm long stainless steel mesh cylinder that functions as a well-defined ion-photon-beam interaction region. This cylinder is electrically isolated and can be biased for the purpose of energy-tagging the product ions produced therein. Beam spatial overlaps are carefully monitored within this region using three translating, two-dimensional slit scanners, with overlap measurements typically taking place immediately before and after each absolute photoionization cross-section

4

measurement. These measurements consist of counting photo-ions at a fixed photon energy and using the photo-ion count rate, primary ion and photon beam intensities and characteristics of their physical interaction (e.g., the beam spatial overlaps and the velocity of the ion beam) to calculate the absolute cross section value for that photon energy. While absolute mode is typically used in this manner, it can also be used to perform spectroscopic energy-scan measurements. The purpose of measuring spectroscopy in absolute mode is to minimize artifacts in the spectra that may arise due to inconsistencies in spatial beam overlaps with low-intensity primary ion beams. In this modified form, photo-ions are counted as the photon energy is stepped through a predetermined range with beam overlap measurements made at discrete photon energies between successive energy range scans.

The photon beam is produced by a 10 cm period, 43 period undulator housed within the 1.9 GeV, 500 mA constant-current electron storage ring of the Advanced Light Source (ALS). A spherical-grating monochromator downstream of the undulator produces a photon beam less than 1 mm wide with a divergence of less than 0.05º. The monochromator at Beamline 10 is equipped with three interchangeable diffraction gratings with an overall photon energy capability of 16.5 eV to 350 eV. The present measurements were made using the low-energy grating which has 380 lines/mm and covers an energy range of 16.5 eV to 85 eV. The photon flux is monitored by a silicon photodiode (IRD, SXUV-100) referenced to a second photodiode from the same manufacturing batch that was absolutely calibrated by the National Institute of Standards and Technology (NIST) and the National Synchrotron Light Source in different photon energy ranges. These photodiode responsivity calibrations permit determination of

incident light intensity with an uncertainty of typically no more than 5%. The beamline

photon flux at 18.2 eV is 2.3×10^{12} photons/sec at 5.5 meV photon energy resolution

which corresponds to a resolving power of approximately 3300. For the present

measurements the photon energy scale was calibrated on a side-branch gas cell

permanently installed at Beamline 10 using well-known doubly-excited, autoionizing He

resonances at 20.049, 21.219, and 21.489 eV [12]. The calibration resulted in a photon

energy uncertainty conservatively estimated to be no more than 10 meV across the entire

photon energy range.

III. RESULTS AND ANALYSIS

A. Measuring and Normalizing the Photoionization Spectrum

The Se^+ photo-ion yield spectrum was assembled from 15 individual scans, each 500

meV wide made with energy steps of 1 meV with 250 meV of overlap between adjacent

scans. The spectrum was compared to an absolute cross section of 4.88 Mb measured at

21.1 eV as reported in Paper I and is in agreement with this value within the experimental

uncertainty. While this absolute cross section was measured at a different photon energy

resolution than the present analysis, it is in a region with no clearly resolved resonances

that is dominated by direct photoionization. The integrated oscillator strength was also

compared to that reported in Paper I, with their oscillator strengths agreeing to within ±

1% across the entire energy range of the present measurements. A comparison of the

high and low resolution absolute cross section measurements is shown in Figure 1. More

detailed resonance structures are visible in the high resolution data where some broad

individual resonances have been clearly resolved into multiple individual features.

FIG. 1. (Color online) Absolute $Se^+ \rightarrow Se^{2+}$ photoionization cross section measured at 5.5 meV photon energy resolution (top panel, present work) and at 28 meV resolution (bottom panel, Paper I [1]). The circle with error bars represents the absolute measurement reported in Paper I. Ground and metastable state ionization thresholds are indicated by vertical bars with dashed lines in the top panel and continued into the bottom panel for reference [17].

In the top panel of Figure 1, broad features are clearly evident below the $^2P^o_{3/2}$ ionization threshold at 18.233 eV. While features in this energy range could be produced by primary ions in long-lived metastable states that are more energetic than the $^2P^o_{3/2}$ state, it is shown in the following section that these features are a result of photoionization by higher-order photons at three times the measured photon energy. Upon close inspection, these features are also apparent in the lower-resolution data.

B. Higher-Order Radiation Analysis

Higher-order radiation produced by the undulator and dispersed by the grating monochromator is a characteristic of synchrotron radiation [13]. While second-order radiation has intensity lobes that are primarily off-axis and can be mitigated by appropriate baffles, third-order radiation is well-collimated and collinear with the first-order output. Third-order radiation is therefore present in the photon beam at all energies and can contribute as much as several percent to the total photon flux. In addition, the measurements are particularly sensitive to third-order radiation at photon energies below 20 eV because of a rapid decrease in both grating efficiency in first order and photo diode quantum efficiency.

Photoionization measurements from 35 to 36.5 eV, or double the energy of the region in question, revealed no apparent structure and only a very small photoionization cross section. However, at triple the energy strong features were measured nearly identical in shape to those seen below the $^2P^o_{3/2}$ threshold, indicating photoionization by third-order radiation was the source of the observed structure. These features are due to $3d \rightarrow np$ transitions corresponding to those seen in the isoelectronic Br^{2+} ion previously measured by Cummings and O'Sullivan [14]. Measurements were made from 53.55 to 56.40 eV and were normalized to an absolute cross-section measurement taken at 54.62 eV as indicated by the circle with error bars in the top panel of Figure 2. Measurements were also made beyond the prominent features but no significant structure was found.

FIG. 2. (Color online) High-resolution Se^+ spectra comparison. Top panel: third-order features measured in first order are normalized to a single absolute cross-section measurement as indicated by the circle with error bars. Bottom panel: the Se^+ spectrum, uncorrected for the effects of higher-order radiation. Metastable state ionization thresholds are indicated by vertical bars with dashed lines in the bottom panel [17].

Using the spectrum from the top panel of Figure 2, the third-order contributions were removed, producing a high-resolution spectrum due to first-order radiation only. Comparison of photoionization rates observed at 18.21 and 54.62 eV indicated that the fraction of third-order light was approximately $5.4\% \pm 2.0\%$. On the surface this is a low percentage, but the order-of-magnitude difference in photodiode sensitivity to first and third-order energies results in an overestimation of the photon flux of up to 70%, thus complicating the measurement of absolute cross section values. Although the 5.4% value

8

could be used to correct the spectrum at 18.21 eV, the photon energy dependence of higher-order light precludes the application of a constant correction to the entire spectrum. Furthermore, second-order radiation is not completely negligible and similarly can contribute to the overestimation of the photon flux. Therefore, the fraction of higher-order radiation as a function of photon energy was estimated by direct measurement of the relative second and third-order radiation intensities utilizing a hemispherical photoelectron spectrometer (Scienta 2002).

The electron transmission efficiency as a function of energy for the hemispherical spectrometer at Beamline 10 was determined following the procedure described in Jauhiainen *et al.* [15]. Relative photoelectron production from p-electron ionization of Ne and Kr gases arising from the first, second, and third harmonics ($h\nu_1$, $h\nu_2 = 2h\nu_1$, and $h\nu_3 = 3h\nu_1$, respectively) were obtained for the beamline at nominal photon energies of 18.227 eV (Kr), 21.670 eV (Kr), and 29.950 eV (Ne). The fluxes Φ_2 and Φ_3 of the second and third harmonics relative to the first-order flux (ν_1) Φ_1 could then be obtained using the known photoionization cross sections in these gases (see Table I) [16]. Using these results, an energy-dependent estimate of the flux ratio was produced for photon energies between 18 and 35 eV and used to account for the overestimation of the first-order flux by the photodiode. This amounted to a correction of $\approx 70\%$ at 18 eV down to $\approx 2\%$ at 35 eV. The final corrected absolute photoionization spectrum is shown in Figure 3 with the third-order features removed and the cross section corrected to account for second- and third-order radiation. Note that the absolute cross section value at 21.1 eV originally reported in Paper I to be 4.88 Mb has been scaled in the same manner and is now 6.14 Mb.

9

TABLE I. Measured flux of the second order (Φ_2) and third order (Φ_3) radiation relative to that of the fundamental (Φ_1).

	18.277 eV (Kr)	21.670 eV (Kr)	29.950 eV (Ne)
Φ_2/Φ_1	0.8 ± 0.4	0.27 ± 0.19	0.6 ± 0.7
Φ_3/Φ_1		3.6 ± 1.8	0.8 ± 0.4

FIG. 3. (Color online) Corrected absolute $Se^+ \rightarrow Se^{2+}$ photoionization cross section measured at 5.5 meV photon energy resolution. Third-order features have been removed and the spectrum has been adjusted to account for higher-order photon flux effects. The large circle with error bars represents the absolute cross-section measurement previously reported in Paper I [1]. Direct ionization thresholds for the ground and metastable states are indicated by dashed vertical lines [17].

C. Rydberg Series Identifications

The NIST Atomic Spectra Database [17] reports the ionization potential of Se^+ to be 21.189 eV and the energy levels of the lowest-lying metastable states of both the primary Se^+ ion and product Se^{2+} ion as indicated in Tables II and III. In the present analysis, the location, energy spacing and apparent series limits of certain Rydberg series of resonances indicated that there must be at least one final state of Se^{2+} lying between the ground state and the $^1D_2$ state reported at 1.616 eV, with the only such candidates being the $^3P_1$ and $^3P_2$ fine structure levels of Se^{2+}. While the NIST database reports these levels as degenerate with the ground state, the NIST source data reported by Moore (1952) [18] does quote energies of 0.216 eV and 0.488 eV above the ground state for the $^3P_1$ and $^3P_2$ levels, respectively. Due to this discrepancy, the online version of the Cowan atomic

10

code available from Los Alamos National Laboratory [19] was used to calculate these levels as verification of the original source data. Using these values as a starting point and allowing them to be free parameters in the Rydberg resonance series analysis resulted in an experimentally-determined $^3P_2$ fine structure energy-level of 0.493 eV ± 0.010 eV above the ground state. No series were found to converge to the $^3P_1$ state, thus experimental verification of this energy level was not possible.

In this analysis, the series limits were initially set using the values reported in the NIST database. After tentative Rydberg series identifications had been made, the series limits were then treated as free parameters with the final series limits determined by the present analysis shown in bold at the bottom of each Rydberg series table. Finally, we note that the NIST-reported energy for the $^1S_0$ state is not referenced to the Se^{2+} ground state and carries a larger (unspecified) uncertainty. The present analysis allows us to provide a measurement of the $^1S_0$ state relative to the other dominant lines in this energy region, with a final value of 3.470 eV ± 0.050 eV.

TABLE II. Energy levels of Se^+ from NIST, the Cowan code, and the present analysis.

Configuration	Term	J	NIST (eV)	Cowan (eV)	Present Analysis (eV)
$[Ar]3d^{10}4s^24p^3$	$^4S^o$	3/2	0	0	0
	$^2D^o$	3/2	1.63265	1.689	1.633 ± 0.025
		5/2	1.70905	1.752	1.709 ± 0.010
	$^2P^o$	1/2	2.85638	2.905	2.854 ± 0.050
		3/2	2.96258	2.990	2.956 ± 0.050
$[Ar]3d^{10}4s^24p^2$	^3P	0	21.1889	21.143	21.189 ± 0.010

TABLE III. Energy levels of Se^{2+} from NIST, the Cowan code, and the present analysis.

Configuration	Term	J	NIST (eV)	Cowan (eV)	Present Analysis (eV)
$[Ar]3d^{10}4s^24p^2$	^3P	0	0	0	0

11

	1	0.216^{*}	0.194	−
	2	0.488^{*}	0.448	0.493 ± 0.010
^{1}D	2	1.6158	1.635	1.620 ± 0.010
^{1}S	0	$3.5249^{\dagger}$	3.524	3.470 ± 0.050

energy levels reported by Moore (1952) [19]

†*no experimental connection was reported between this level and the other levels of the spectrum has been made previously, and this value carries a larger (unspecified) uncertainty.*

In Figure 4, the numbering scheme that is used to refer to Rydberg series resonances in the following tables is shown. In some instances it was determined after the numbering had taken place that certain poorly resolved features were actually multiple resonances. In such cases a lettering designation was added.

FIG. 4. (Color online) Numerical designations used in the Rydberg resonance series identification tables.

Figure 5 is an expanded view of the energy region between the $^{2}P^{o}_{3/2}$ threshold and the $4s^{2}4p^{2}$ (^{1}D) series limits of the ^{2}P states where four Rydberg series have been identified. One series is due to $4p \rightarrow nd$ transitions with a ^{1}D series limit and has been identified originating from the $^{2}P^{o}_{3/2}$ state as indicated by solid up and down triangles. These identifications differ only in their coupling between the core and the excited electron ($^{2}P_{1/2}$ and ^{2}S). The same series has been identified originating from the $^{2}P^{o}_{1/2}$ state as indicated by hollow up and down triangles which again differ only in their coupling terms ($^{2}P_{1/2}$ and ^{2}S). A second series due to to $4p \rightarrow nd$ transitions has been identified, but with a $^{3}P_{2}$ series limit. This series originates from both the $^{2}P^{o}_{3/2}$ and $^{2}P^{o}_{1/2}$ states and is identified by solid and hollow diamonds, respectively. A

series due to $4p \rightarrow ns$ transitions with a ^{1}D series limit has been identified originating from the $^2P^o_{3/2}$ and $^2P^o_{1/2}$ states (half-filled triangles). The last identified series in this region is due to $4p \rightarrow nd$ transitions with a ^{1}S series limit originating from both ^{2}P initial states (solid and hollow squares). The limits of this last series are beyond the $^4S^o_{3/2}$ threshold so only the initial $n = 5$ resonances are shown in Figure 5, with the remainder shown in Figure 7. The details of these series are listed in Tables IV through VIII.

FIG. 5. (Color online) Rydberg series of resonances due to $4p \rightarrow nd$ and ns transitions converging to the $4s^24p^2$ ($^1D_2$, $^3P_2$, and $^1S_0$) series limits of Se^{2+} and originating from the $^2P^o_{3/2}$ and $^2P^o_{1/2}$ metastable states of Se$^+$ are identified. Metastable state ionization thresholds are indicated by vertical bars with dashed lines [17].

Each tabulated resonance is identified by peak number, principal quantum number, n, resonance energy, and quantum defect parameter, δ, which is a quantification of the deviation of the true energy of an excited electron in a Rydberg atom from the hydrogenic model. The particular values of δ were found analytically and are a function of the principal quantum number and excitation energy of each resonance and are therefore related to the energy uncertainty and resolution of these measurements. The values of δ in this analysis typically approach zero with increasing principal quantum number, but even in cases where they do not, the quantum defect parameter has a vanishingly small effect on predicted resonance energies at high n. Due to these characteristics, individual uncertainties in the quantum defect parameter have not been

13

quoted and the tabulated δ values can be considered accurate within the energy uncertainty of these measurements. In addition, within the experimental energy uncertainties, positive delta values are allowable for the high-n resonances for which negative quantum defect parameters were determined. Lastly, in certain instances some resonances are not resolvable, either due to interference from other series or to limitations in photon energy resolution at high n values. In such instances, tabulated peak numbers have been omitted but energies and δ values have been included to indicate predicted resonance energies.

TABLE IV. Rydberg series of resonances due to $4p \rightarrow nd$ transitions from the $^2P^o_{3/2}$ metastable state of Se$^+$ converging to the $^1D_2$ series limit in Se^{2+}.

Initial Se$^+$ State: $4s^24p^3$ ($^2P^o_{3/2}$)								
Rydberg Series					**Rydberg Series**			
$4s^24p^2$ ($^1D_2$) nd ($^2P_{1/2}$)					$4s^24p^2$ ($^1D_2$) nd (^2S)			
n	Energy (eV)	δ	Peak #		n	Energy (eV)	δ	Peak #
6	18.249	0.175	1		6	18.296	0.088	5
7	18.688	0.165	26		7	18.710	0.100	27
8	18.970	0.150	32		8	18.990	0.150	33
9	19.158	0.150	38		9	19.169	0.088	39
10	19.294	0.130	44		10	19.302	0.060	45
11	19.392	0.130	48		11	19.396	0.088	48
12	19.469	0.100	51		12	19.470	0.080	51
13	19.537	-0.125	55		13	19.528	0.070	54
14	19.581	-0.150	58		14	19.574	0.060	57
15	19.616	-0.150	60		15	19.613	0	60
∞	**19.853**	-	-		∞	**19.853**	-	-

TABLE V. Rydberg series of resonances due to $4p \rightarrow nd$ and ns transitions from the $^2P^o_{3/2}$ metastable state of Se$^+$ converging to the $^3P_2$ (nd) and $^1D_2$ (ns) Se^{2+} series limits.

Initial Se$^+$ State: $4s^24p^3$ ($^2P^o_{3/2}$)								
Rydberg Series					**Rydberg Series**			
$4s^24p^2$ ($^3P_2$) nd					$4s^24p^2$ ($^1D_2$) ns			
n	Energy (eV)	δ	Peak #		n	Energy (eV)	δ	Peak #
11	18.273	0.040	3		7	18.560	0.512	19
12	18.342	0.090	7a		8	18.886	0.500	31
13	18.401	0.070	10b		9	19.102	0.490	36
14	18.446	0.055	12		10	19.250	0.500	42

14

n	Energy (eV)	δ	Peak #		n	Energy (eV)	δ	Peak #
15	18.482	0.065	14		11	19.359	0.500	47
16	18.512	0.060	16		12	19.442	0.500	50
17	18.537	0.040	17		13	19.505	0.500	52b
18	18.560	-0.080	19		14	19.554	0.500	56
19	18.575	0.040	20		15	19.594	0.500	59
20	18.589	0.040	21		16	19.627	0.500	-
21	18.602	0.040	22		17	19.653	0.500	-
22	18.613	0.040	23		18	19.675	0.500	-
-	-	-	-		19	19.694	0.500	-
∞	**18.726**	-	-		∞	**19.853**	-	-

TABLE VI. Rydberg series of resonances due to $4p \rightarrow nd$ transitions from the $^2P^o_{1/2}$ metastable state of Se$^+$ converging to the $^1D_2$ series limit in Se^{2+}.

Initial Se$^+$ State: $4s^2 4p^3$ ($^2P^o_{1/2}$)								
Rydberg Series					**Rydberg Series**			
$4s^2 4p^2$ ($^1D_2$) nd ($^2P_{1/2}$)					$4s^2 4p^2$ ($^1D_2$) nd (^2S)			
n	Energy (eV)	δ	Peak #		n	Energy (eV)	δ	Peak #
6	18.351	0.175	7b		6	18.393	0.097	10a
7	18.790	0.165	28		7	18.816	0.087	29
8	19.071	0.152	34		8	19.077	0.125	35
9	19.262	0.140	43		9	19.264	0.125	43
10	19.395	0.140	48		10	19.396	0.135	48
11	19.494	0.130	52a		11	19.495	0.125	52a
12	19.571	0.100	57		12	19.571	0.100	57
13	19.633	0	61		13	19.632	0.025	61
14	19.683	-0.150	64		14	19.681	-0.100	64
15	19.718	-0.150	66		15	19.718	-0.150	66
-	-	-	-		16	19.749	-0.240	68a
∞	**19.955**	-	-		∞	**19.955**	-	-

TABLE VII. Rydberg series of resonances due to $4p \rightarrow nd$ and ns transitions from the $^2P^o_{1/2}$ metastable state of Se$^+$ converging to the $^3P_2$ (nd) and $^1D_2$ (ns) limits in Se^{2+}.

Initial Se$^+$ State: $4s^2 4p^3$ ($^2P^o_{1/2}$)								
Rydberg Series					**Rydberg Series**			
$4s^2 4p^2$ ($^3P_2$) nd					$4s^2 4p^2$ ($^1D_2$) ns			
n	Energy (eV)	δ	Peak #		n	Energy (eV)	δ	Peak #
11	18.375	0.040	9		7	18.667	0.500	25
12	18.448	0.040	12		8	18.991	0.488	33
13	18.504	0.040	15		9	19.207	0.470	41
14	18.552	-0.030	18		10	19.357	0.460	47
15	18.588	-0.050	21		11	19.467	0.440	51
16	18.617	-0.060	23		12	19.549	0.420	56
17	18.642	-0.120	24		13	19.613	0.380	60
18	18.666	-0.350	25		14	19.663	0.355	63
-	-	-	-		15	19.702	0.340	65
∞	**18.828**	-	-		∞	**19.955**	-	-

TABLE VIII. Rydberg series of resonances due to $4p \rightarrow nd$ transitions from both the $^2P^o_{3/2}$ and $^2P^o_{1/2}$ metastable states of Se^+ converging to $^1S_0$ series limits in Se^{2+}.

Initial Se⁺ State: $4s^24p^3$ ($^2P^o_{3/2}$)				Initial Se⁺ State: $4s^24p^3$ ($^2P^o_{1/2}$)			
Rydberg Series				Rydberg Series			
$4s^24p^2$ ($^1S_0$) nd (^2D)				$4s^24p^2$ ($^1S_0$) nd (^2D)			
n	Energy (eV)	δ	Peak #	n	Energy (eV)	δ	Peak #
5	19.320	0.221	46	5	19.468	0.174	51
6	20.076	0.217	80	6	20.202	0.174	83
7	20.530	0.188	92	7	20.637	0.174	96
8	20.816	0.165	102	8	20.922	0.150	107a
9	21.009	0.145	112	9	21.116	0.110	116b
10	21.149	0.088	117	10	21.238	0.200	120
11	21.255	-0.025	121	11	21.331	0.280	124d
12	21.325	0	124c	12	21.422	0.075	128
13	21.383	-0.050	126	-	-	-	-
∞	**21.703**	-	-	∞	**21.805**	-	-

Figure 6 is an expanded view of the energy region between the $^2D^o_{5/2}$ threshold and the $4s^24p^2$ (^1D) series limits of the ^2D states where three Rydberg series have been identified. Two series are due to $4p \rightarrow nd$ transitions; one with a $^1D_2$ series limit and the other with a $^3P_2$ series limit. Each of these series originates from both the $^2D^o_{5/2}$ and $^2D^o_{3/2}$ states (solid and hollow down triangles for the $^1D_2$ series and diamonds for the $^3P_2$ series). The series originating from the $^2D^o_{3/2}$ state with a $^3P_2$ series limit (hollow diamonds) is very difficult to differentiate from the other series and the direct ionization background and is therefore only a tentative identification. The final series in this region is attributed to $4p \rightarrow ns$ transitions with a ^1D series limit originating from the $^2D^o_{5/2}$ state (solid up triangles) and the $^2D^o_{3/2}$ state (hollow up triangles). The details of these series are listed in Tables IX through XI.

FIG. 6. (Color online) Rydberg series of resonances due to $4p \rightarrow nd$ and ns transitions converging to the $4s^24p^2$ ($^1D_2$ and $^3P_2$) series limits of Se^{2+} originating from the $^2D^o_{5/2}$ and $^2D^o_{3/2}$ metastable states of Se^+ are identified. Metastable and ground state ionization thresholds are indicated by vertical bars with dashed lines [17].

TABLE IX. Rydberg series of resonances due to $4p \rightarrow nd$ transitions from the $^2D^o_{5/2}$ metastable state of Se^+ converging to the $^1D_2$ and $^3P_2$ series limits in Se^{2+}.

Initial Se+ State: $4s^24p^3$ ($^2D^o_{5/2}$)							
Rydberg Series $4s^24p^2$ ($^1D_2$) nd (^2D)				Rydberg Series $4s^24p^2$ ($^3P_2$) nd			
n	Energy (eV)	δ	Peak #	n	Energy (eV)	δ	Peak #
6	19.501	0.166	52b	11	19.523	0.003	54
7	19.935	0.166	77	12	19.595	0.003	59
8	20.213	0.166	84	13	19.651	0.003	62
9	20.403	0.166	88	14	19.697	-0.040	65
10	20.537	0.166	93	15	19.733	-0.050	67
11	20.636	0.166	96	16	19.764	-0.110	68b
12	20.711	0.166	98	17	19.789	-0.200	69
13	20.770	0.156	100	18	19.811	-0.350	70
14	20.816	0.150	102	19	19.827	-0.320	71
15	20.853	0.146	103	20	19.842	-0.300	72
16	20.884	0.135	104	21	19.855	-0.400	73
17	20.909	0.110	106	22	19.865	-0.400	74a
18	20.931	0.080	107	23	19.874	-0.450	74b
19	20.948	0.050	108	-	-	-	-
20	20.963	0.050	109	-	-	-	-
21	20.976	0.050	110	-	-	-	-
22	20.987	0.050	111	-	-	-	-
23	20.997	0	112	-	-	-	-
∞	**21.100**	-	-	∞	**19.973**	-	-

TABLE X. Rydberg series of resonances due to $4p \rightarrow nd$ transitions from the $^2D^o_{3/2}$ metastable state of Se^+ converging to the $^1D_2$ and $^3P_2$ series limits in Se^{2+}.

Initial Se+ State: $4s^24p^3$ ($^2D^o_{3/2}$)							
Rydberg Series $4s^24p^2$ ($^1D_2$) nd (^2D)				Rydberg Series $4s^24p^2$ ($^3P_2$) nd			
n	Energy (eV)	δ	Peak #	n	Energy (eV)	δ	Peak #
6	19.572	0.175	57	11	19.595	0.051	59
7	20.009	0.170	79	12	19.668	0.051	63
8	20.289	0.168	86	13	19.724	0.051	66
9	20.479	0.164	90	14	19.770	0.035	68b

n	Energy (eV)	δ	Peak #		n	Energy (eV)	δ	Peak #
10	20.613	0.170	95		15	19.807	0.020	70
11	20.713	0.160	98		16	19.835	0.051	-
12	20.788	0.160	101		17	19.860	0.051	73
13	20.846	0.155	103		18	19.880	0.051	-
14	20.892	0.150	105		19	19.897	0.051	-
15	20.929	0.150	107		20	19.912	0.051	-
16	20.960	0.135	109		21	19.925	0.051	-
17	20.985	0.130	111		22	19.936	0.051	-
18	21.006	0.120	112		23	19.946	0.051	-
19	21.024	0.110	113		24	19.954	0.051	-
20	21.039	0.100	114		25	19.962	0.051	-
21	21.053	0	115		-	-	-	-
22	21.064	0	116a		-	-	-	-
23	21.073	0	116a		-	-	-	-
24	21.082	0	116a		-	-	-	-
25	21.089	0	116a		-	-	-	-
∞	**21.176**	-	-		∞	**20.049**	-	-

TABLE XI. Rydberg series of resonances due to $4p \rightarrow ns$ transitions from both the **$^2D^o_{5/2}$** and **$^2D^o_{3/2}$** metastable states of Se$^+$ converging to $^1D_2$ series limits in Se^{2+}.

Initial Se$^+$ State: $4s^24p^3$ ($^2D^o_{5/2}$)					Initial Se$^+$ State: $4s^24p^3$ ($^2D^o_{3/2}$)			
Rydberg Series $4s^24p^2$ ($^1D_2$) ns (^2D)					Rydberg Series $4s^24p^2$ ($^1D_2$) ns (^2D)			
n	Energy (eV)	δ	Peak #		n	Energy (eV)	δ	Peak #
7	19.811	0.502	70		7	19.890	0.495	75
8	20.135	0.490	81		8	20.214	0.480	84
9	20.350	0.480	87		9	20.428	0.470	89
10	20.501	0.470	91		10	20.576	0.480	94
11	20.610	0.460	95		11	20.685	0.470	97
12	20.690	0.480	97		12	20.770	0.420	100
13	20.753	0.480	99		13	20.830	0.460	-
14	20.803	0.460	-		14	20.883	0.380	104
15	20.846	0.360	103		15	20.922	0.360	107
16	20.882	0.200	104		16	20.955	0.300	109
17	20.909	0.100	106		17	20.985	0.100	111
18	20.932	0	107		18	21.008	0	112
19	20.949	0	108		19	21.025	0	113
20	20.964	0	109		20	21.040	0	114
21	20.977	0	110		21	21.053	0	115
22	20.988	0	111		22	21.064	0	116a
23	20.997	0	-		23	21.073	0	116a
∞	**21.100**	-	-		∞	**21.176**	-	-

Figure 7 is an expanded view of the region from just below the $^2D^o_{5/2}$ metastable-state

threshold to beyond the $^4S^o_{3/2}$ ground state threshold where one additional Rydberg series

of resonances was identified. This series is attributed to $4s \rightarrow np$ transitions originating

from the $^4S^o_{3/2}$ ground state with a $^3P_2$ series limit (solid triangles). The additional series

indicated in the figure was previously described as originating from the $^2P^o_{3/2}$ and $^2P^o_{1/2}$

states and is attributed to $4p \rightarrow nd$ transitions with $^1S_0$ series limit (solid and hollow

squares, see Figure 5 and Table VIII). The details of the series originating from the $^4S^o_{3/2}$

ground state are listed in Table XII.

FIG. 7. (Color online) A single Rydberg series of resonances due to $4s \rightarrow np$ transitions

converging to the $4s^24p^2$ ($^3P_2$) series limit is identified originating from the $^4S^o_{3/2}$ ground state. In

addition, the series originating from both ^2P metastable states due to $4p \rightarrow nd$ transitions

converging to $4s^24p^2$ ($^1S_0$) series limit are shown (solid and hollow squares). The ionization

thresholds of the $^4S^o_{3/2}$ ground state and ^2D metastable states are indicated by vertical bars with

dashed lines [17].

TABLE XII. Rydberg series of resonances due to $4p \rightarrow nd$ transitions from the $^4S^o_{3/2}$ ground

state converging to the $^3P_2$ series limit in Se^{2+}.

Initial Se$^+$ State: $4s^24p^3$ ($^4S^o_{3/2}$)			
Rydberg Series			
$4s^24p^2$ ($^3P_2$) nd			
n	Energy (eV)	δ	Peak #
11	21.215	0.210	119
12	21.219	0.210	123
13	21.349	0.210	125
14	21.396	0.210	127
15	21.433	0.210	129
16	21.464	0.210	131
17	21.489	0.210	132
18	21.510	0.210	133
19	21.528	0.210	134
20	21.543	0.210	135

21	21.556	0.210	136
22	21.567	0.210	137
23	21.577	0.210	138
24	21.586	0.210	139
25	21.593	0.210	140
∞	**21.682**	-	-

In Figure 8 the *4p → ns* series with a ^{1}D series limit is plotted for both the $^2D^o_{5/2}$ and $^2D^o_{3/2}$ initial states. The resonance energies for this series are plotted versus their effective quantum number, n_{eff}, which is defined as

$$n_{eff} = n - \delta.$$

This comparison is provided as an example of the behavior of identified Rydberg series originating from different initial states. In each case in the present analysis where series originate from more than one state, they demonstrate similar behaviors to those in Figure 8 indicating that the resonance identifications and quantum defect behaviors are consistent. The one exception is the *4p → nd* transition series originating from the $^2P^o_{1/2}$ state with a $^3P_2$ series limit. The behavior of this series deviates at high *n* from the same series originating from the $^2P^o_{3/2}$ state. Two factors that may explain this deviation are the very low intensity of the series resonances at high *n*, and the final few (weakest) resonances are overlapped by the initial *n* = 7 resonances of the *4p → ns* transitions with a ^{1}D series limit (see Figure 5). The combination of these two factors makes accurate determination of quantum defect values for this series at very high *n* values difficult.

FIG. 8. (Color online) Resonance energies versus effective quantum numbers for the Rydberg Series arising from $4p \rightarrow ns$ transitions with a ^{1}D series limit originating from the $^2D^o_{5/2}$ and $^2D^o_{3/2}$ states.

IV. SUMMARY AND CONCLUSIONS

Absolute single photoionization cross-section measurements for Se$^+$ in the region of the ground state threshold (17.75 to 21.85 eV) at a photon energy resolution of 5.5 meV have been presented. The primary ion beam consisted of an unknown admixture of the $^2P^o_{3/2}$, $^2P^o_{1/2}$, $^2D^o_{5/2}$, and $^2D^o_{3/2}$ metastable states and the $^4S^o_{3/2}$ ground state. Analysis of the autoionizing resonance features produced detailed identifications of numerous Rydberg series of resonances where as many as 19 members of a series were identified. The Rydberg resonance series identifications included comparative analysis of the quantum defect parameter from like transitions originating from related fine structure components which strongly supports the series identifications. The ability to resolve such structure and thus accurately identify the many resonance series required high spectral resolving power. These measurements improve on the already detailed measurements reported in Paper I and permitted the experimental determination of the Se^{2+} $^3P_2$ and $^1S_0$ state energies. The present analysis also revealed features which were determined to result from a small fraction of higher-order radiation in the photon beam. These features were removed and the photoionization spectrum was corrected to account for errors in the determination of absolute cross section values caused by this higher-order radiation. This produced a quantifiable measurement of the effects of higher-order radiation on absolute photoionization cross-section measurements at ALS Beamline 10.0.

21

ACKNOWLEDGEMENTS

[1] N. C. Sterling, D. A. Esteves, R. C. Bilodeau, A. L. D. Kilcoyne, E. C. Red, R. A. Phaneuf and A. Aguilar, *J. Phys. B: At. Mol. Opt. Phys.* **44**, 025701(2011). (Paper I)

[2] N. C. Sterling, and H. L. Dinerstein, *Astrophys. J. Suppl. Ser.*, **174**, 158 (2008).

[3] R.D. Blum, and P.J. McGregor, *Astron. J.*, **135**, 1708 (2008).

[4] L. Vanzi, G. Cresci, E. Telles, and J. Melnick, *Astron. Astrophys.* **486**, 393 (2008).

[5] N. C. Sterling, H. L. Dinerstein, and T.R. Kallman, *Astrophys. J. Suppl. Ser.* **169**, 37 (2007).

[6] N. C. Sterling, M. C. Witthoeft, D. A. Esteves, R. C. Bilodeau, A. L. D. Kilcoyne, E. C. Red, R. A. Phaneuf, G. Alna'washi, and A. Aguilar, *Can. J. Phys.*, in press arXiv:1011.6311 (2011).

[7] I. C. Lyon, B. Peart, J. B. West, and K. Dolder, *J. Phys. B: At. Mol. Phys.* **19**, 4137 (1986).

[8] A. M. Covington, A. Aguilar, I. R. Covington, M. F. Gharaibeh, G. Hinojosa, C. A. Shirley, R. A. Phaneuf, I. Álvarez, C. Cisneros, I. Dominguez-Lopez, M. M Sant'Anna, A. S. Schlachter, B. M. McLaughlin, and A. Dalgarno, *Phys. Rev. A* **66**, 062710 (2002).

[9] G. Alna'washi, M. Lu, M. Habibi, A.L.D. Kilcoyne, A. S. Schlacter, C. Cisneros, B. M. McLaughlin, and R. A. Phaneuf, *Phys. Rev. A* **81**, 053416 (2010).

[10] F. Broetz, R. Trassl, R. W. McCullough, W. Arnold, and E. Salzborn, *Phys. Scr.* **T92**, 278 (2001).

[11] R. Trassl , W. R. Thompson , F. Broetz , M. Pawlowsky, R. W. McCullough , and E. Salzborn, *Phys. Scr.* **T80B**, 504 (1999).

[12] M. Domke, K. Schulz, G. Remmers, G. Kaindl, and D. Wintgen, *Phys. Rev. A* **53**, 1424 (1996).

[13] D. Attwood, *Soft X-Rays and Extreme Ultraviolet Radiation* (Cambridge University Press, New York, QC482.G68A88, 1999), P. 141.

[14] A. Cummings, and G. O'Sullivan, *Phys. Rev. A* **54**, 1 (1996).

[15] J. Jauhiainen, A. Ausmees, A. Kivimki, S.J. Osborne, A. Naves de Brito, S. Aksela, S. Svensson, H. Aksela, *J. Electron Spectrosc. Relat. Phenom.* **69**, 181 (1994).

[16] U. Becker and D.A. Shirley, *VUV and Soft X-Ray Photoionization,* Plenum Press (New York, 1996).

[17] Y. Ralchenko, A.E. Kramida, J. Reader, and NIST ASD Team, *NIST Atomic Spectra Database* (version 3.1.5), URL: http://physics.nist.gov/asd3 , National Institute of Standards and Technology, Gaithersburg, MD (2008).

[18] C.E. Moore, *Atomic Energy Levels, Vol. 2*, NBS Circular, **467** (Washington, DC, NBS, 1952).

[19] R. D. Cowan, *The Theory of Atomic Structure and Spectra* (University of California Press, Berkeley (1981). URL:http://aphysics2.lanl.gov/tempweb/
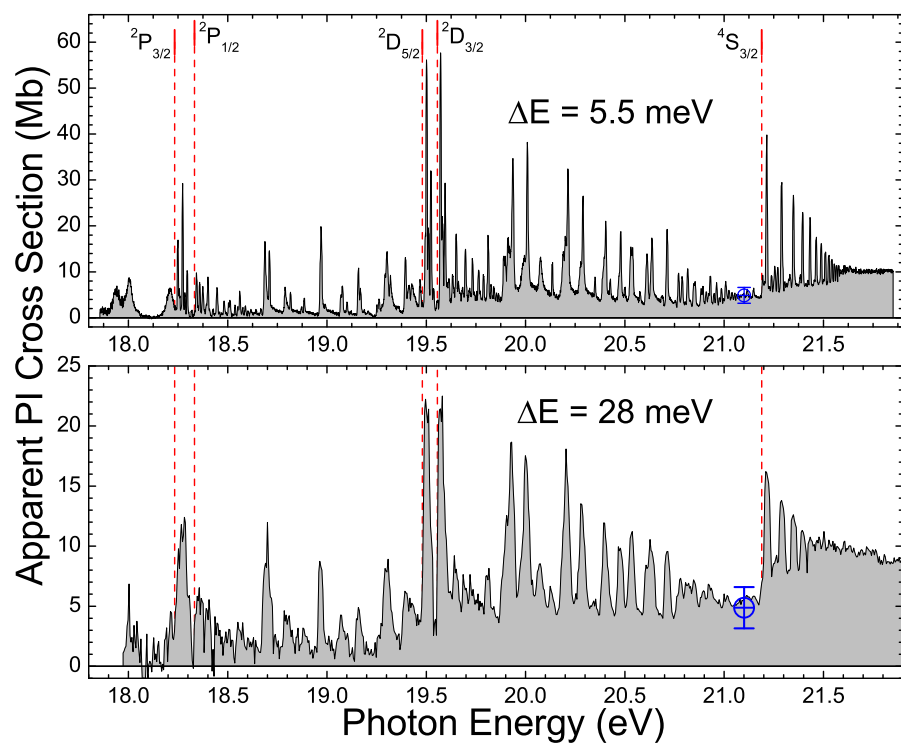
Figure 1   AD10800   31MAY2011
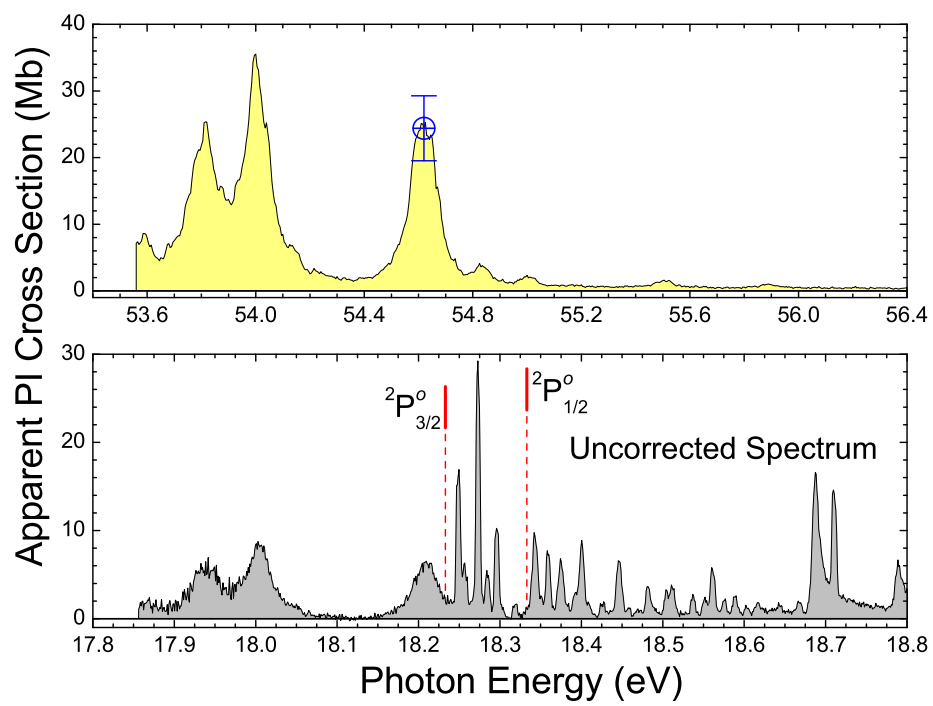
Figure 2   AD10800   31MAY2011
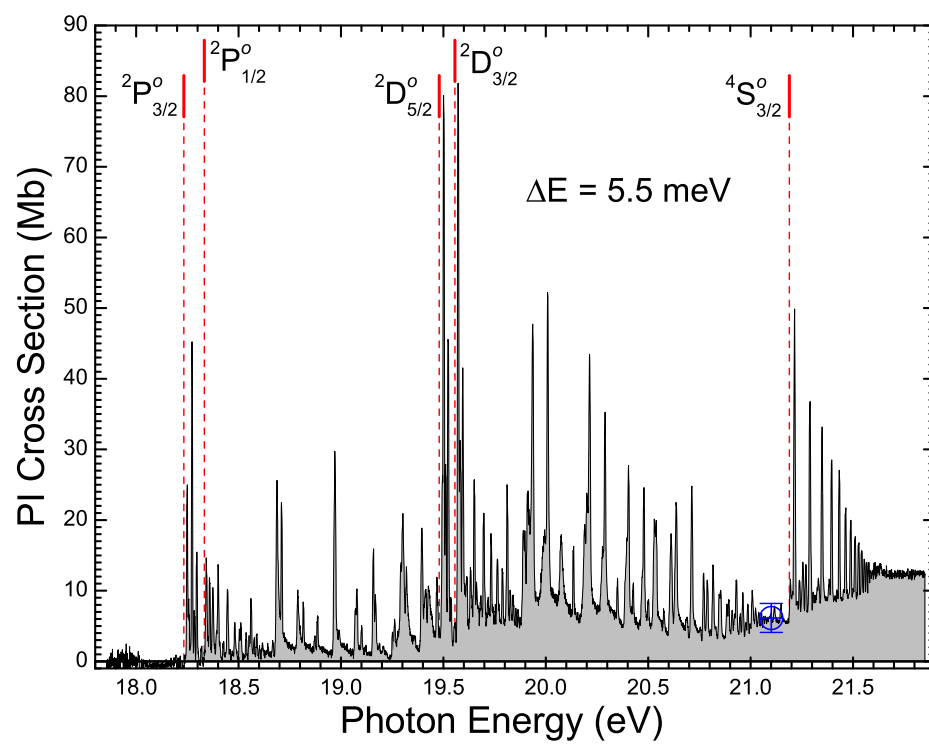
Figure 3   AD10800   31MAY2011
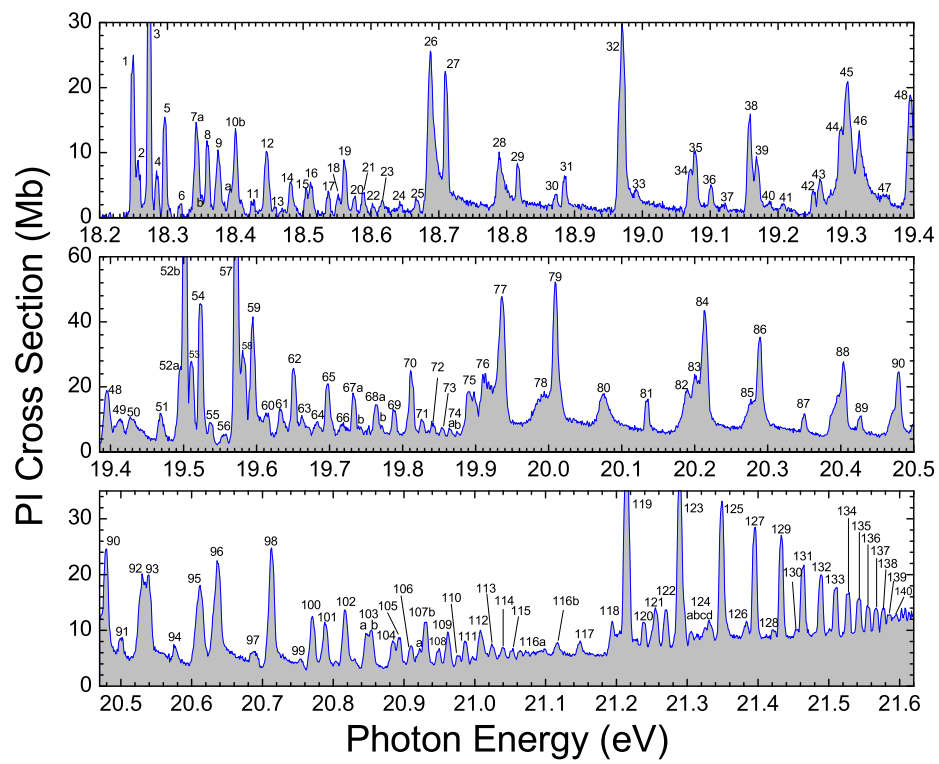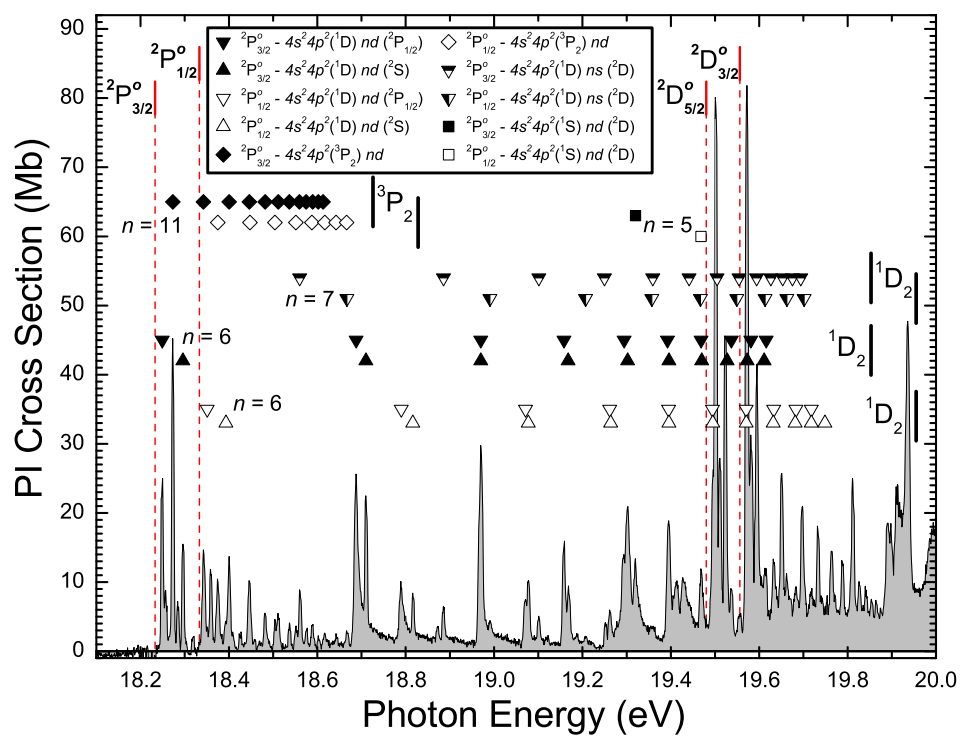
Figure 4   AD10800   31MAY2011
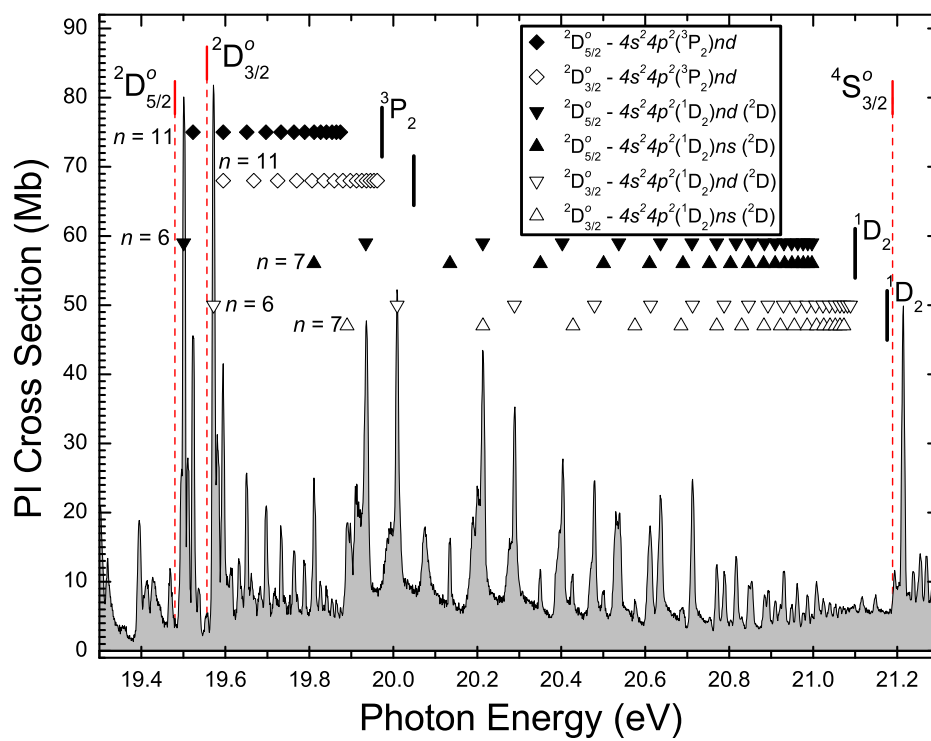
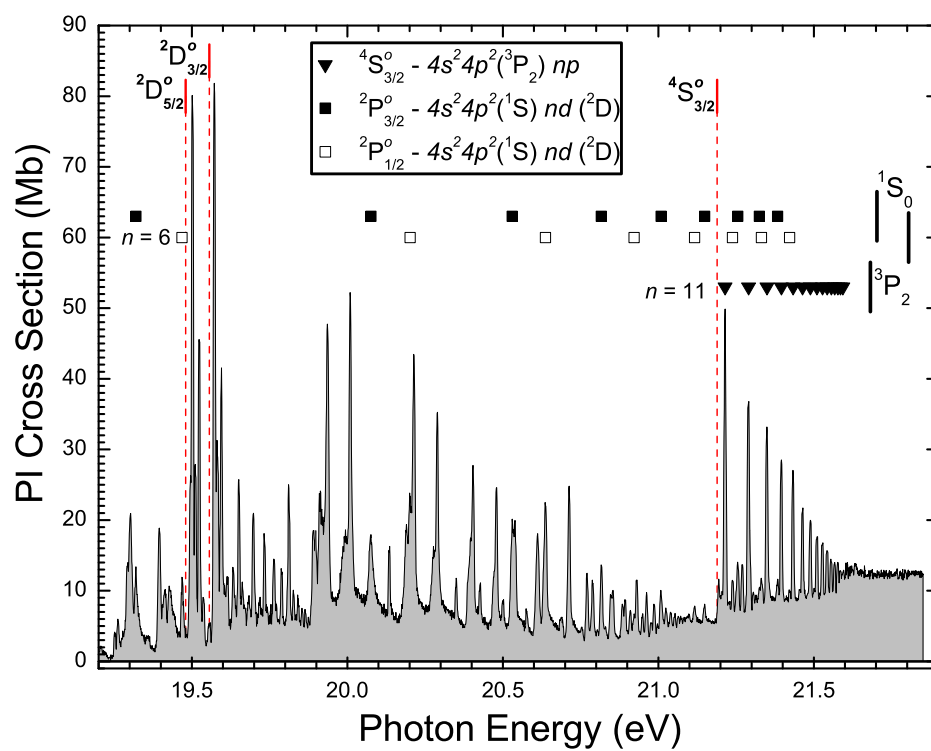Figure 5   AD10800   31MAY2011

Figure 6   AD10800   31MAY2011

Figure 7   AD10800   31MAY2011
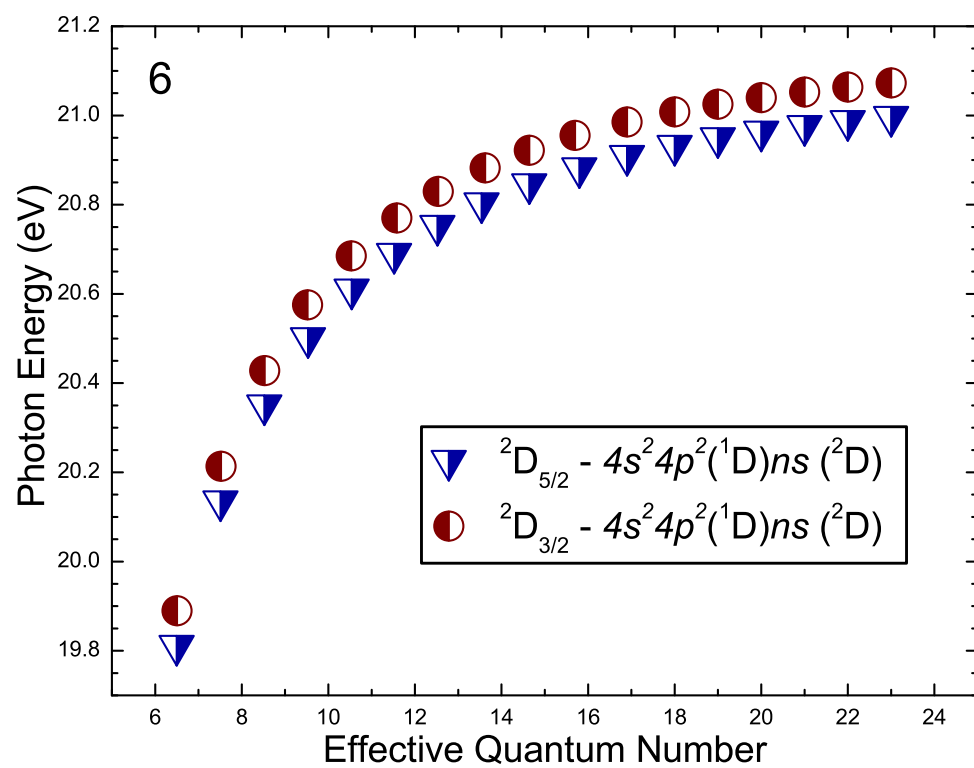
6

$^2D_{5/2} - 4s^24p^2(^1D)ns\ (^2D)$

$^2D_{3/2} - 4s^24p^2(^1D)ns\ (^2D)$

Figure 8   AD10800   31MAY2011